Atmos. Meas. Tech. Discuss., 6, 9297–9346, 2013
www.atmos-meas-tech-discuss.net/6/9297/2013/
doi:10.5194/amtd-6-9297-2013

Atmospheric Measurement Techniques Discussions
Open Access

Retrieval of aerosol backscatter, extinction, and lidar ratio from Raman lidar with optimal estimation

A. C. Povey[1], **R. G. Grainger**[1], **D. M. Peters**[1], **and J. L. Agnew**[2]

[1]Atmospheric, Oceanic, and Planetary Physics, University of Oxford, Parks Road, Oxford, OX1 3PU, UK
[2]STFC Rutherford-Appleton Laboratory, Harwell, Oxford, OX11 0QX, UK

Received: 29 August 2013 – Accepted: 18 October 2013 – Published: 30 October 2013

Correspondence to: A. C. Povey (povey@atm.ox.ac.uk)

Published by Copernicus Publications on behalf of the European Geosciences Union.

Abstract

Optimal estimation retrieval is a form of non-linear regression which determines the most probable circumstances that produced a given observation, weighted against any prior knowledge of the system. This paper applies the technique to the estimation of aerosol backscatter and extinction (or lidar ratio) from two-channel Raman lidar observations. It produces results from simulated and real data consistent with existing Raman lidar analyses and additionally returns a more rigorous estimate of its uncertainties while automatically selecting an appropriate resolution without the imposition of artificial constraints. Backscatter is retrieved at the instrument's native resolution with an uncertainty between 2 and 20 %. Extinction is less well constrained, retrieved at a resolution of 0.1–1 km depending on the quality of the data. The uncertainty in extinction is > 15 %, in part due to the consideration of short one-minute integrations, but is comparable to fair estimates of the error when using the standard Raman lidar technique.

The retrieval is then applied to several hours of observation on 19 April 2010 of ash from the Eyjafjallajökull eruption. A highly depolarizing ash layer is found with a lidar ratio of 20–30 sr, much lower values than observed by previous studies. This potentially indicates a growth of the particles after 12–24 h within the planetary boundary layer. A lower concentration of ash within a residual layer exhibited a backscatter of 10 Mm^{-1} sr^{-1} and lidar ratio of 40 sr.

1 Introduction

Aerosols impact the Earth's radiation budget both directly, by reflecting solar radiation back into space (Haywood and Shine, 1995), and indirectly, by altering the properties and distribution of clouds (Lohmann and Feichter, 2005) or reacting with other species (Colbeck, 1998). The lack of knowledge about the global distribution and composition of aerosols is currently the single greatest source of uncertainty in estimates of net

Discussion Paper | Discussion Paper | Discussion Paper | Discussion Paper |

radiative forcing and therefore is a factor in the ability to predict the impacts of climate change (IPCC, 2007).

Lidar (light detection and ranging) is an active remote sensing technique for observing the distribution of molecules and particles in the atmosphere as a function of height by means of the light they backscatter from a laser beam. The name intentionally emulates radar as both techniques use the time-of-flight of a pulsed source to deduce the distance to the scatterer (Fugii and Fukuchi, 2005). Despite its exceptionally high spatial and temporal resolution, lidar is not as widely applied as other techniques in the study of aerosol. With the launch of a space-based lidar (Vaughan et al., 2004) and the development of networks across Northern America (Welton et al., 2001), Europe (Pappalardo et al., 2005), and Asia (Sugimoto et al., 2008), there is an increasing volume of under-used lidar data.

The energy observed by a lidar is a function of the extinction and backscattering coefficients – the cross-section per unit volume to either attenuate the beam or to scatter light directly back towards the instrument. These coefficients are functions of the microphysical properties of the aerosol present, such as refractive index and size distribution. Deriving such properties directly is possible, but the problem is very poorly constrained. Its solution either requires a greater number of measurements, such as a multi-wavelength system (Müller et al., 1999), or further assumptions about the scatterers. These complexities are disregarded here in favour of the better-constrained estimation of extinction and backscatter.

Optimal estimation retrieval is a form of non-linear regression which determines the most probable circumstances that produced a given observation, weighted against any prior knowledge of the system. For several decades, it has been successfully applied to the analysis of satellite (e.g. Marks and Rodgers, 1993; Li et al., 2008; Watts et al., 2011), radar (Grant et al., 2004), and ground-based radiometer observations (e.g. Guldner and Spankuch, 2001) but has not seen substantial use within the lidar community. This paper applies the technique to the estimation of aerosol extinction and backscatter from two-channel Raman lidar observations. The retrieval processes

AMTD
6, 9297–9346, 2013

the entire profile simultaneously, making optimal use of the information available and choosing the most appropriate vertical resolution for the result while fully characterising the covariant error due to measurement noise, model error, and other assumptions. The use of a widely-recognised retrieval algorithm which is less dependant on ad hoc corrections and assumptions while providing rigorous error estimation brings the analysis of Raman lidar data more in line with modern retrieval theory.

Section 2 outlines the retrieval algorithm and existing analysis methods. Section 3 evaluates the retrieval's performance against existing techniques with simulated data and considers the error budget. Section 4 applies the algorithm to observations while Sect. 5 provides some conclusions.

2 Methods

2.1 Optimal estimation retrieval

As outlined in Rodgers (2000), optimal estimation solves the inverse problem,

$$\boldsymbol{y} = \boldsymbol{F}(\boldsymbol{x}, \boldsymbol{b}) + \boldsymbol{\epsilon}, \tag{1}$$

where $\boldsymbol{y}$ is a column vector describing the measurements; $\boldsymbol{\epsilon}$ gives the noise on that measurement; and the forward model $\boldsymbol{F}(\boldsymbol{x}, \boldsymbol{b})$ translates a state of the instrument and atmosphere, summarised by unknown parameters $\boldsymbol{x}$ and known parameters $\boldsymbol{b}$, into a simulated measurement.

Approximating the probability density function (PDF) for all quantities as Gaussian and using Bayes' Theorem, the probability that the system has a state $\boldsymbol{x}$ given the measurement $\boldsymbol{y}$ can be written as,

$$-2 \ln \mathrm{P}(\boldsymbol{x}|\boldsymbol{y}) = [\boldsymbol{y} - \boldsymbol{F}(\boldsymbol{x}, \boldsymbol{b})]^T \mathbf{S}_\epsilon^{-1} [\boldsymbol{y} - \boldsymbol{F}(\boldsymbol{x}, \boldsymbol{b})] + [\boldsymbol{x} - \boldsymbol{x}_\mathrm{a}]^T \mathbf{S}_\mathrm{a}^{-1} [\boldsymbol{x} - \boldsymbol{x}_\mathrm{a}], \tag{2}$$

where the covariance matrix $\mathbf{S}_\epsilon$ describes the random experimental error and $\boldsymbol{x}_\mathrm{a}$ is the a priori, the state expected before the measurement is made. The uncertainty in

AMTD
6, 9297–9346, 2013

that expectation is described by the a priori covariance $\mathbf{S}_a$. The quantity $-2\ln P(\boldsymbol{x}|\boldsymbol{y})$ is hereafter referred to as the cost as it measures the goodness of fit for a solution. Good models should have a cost approximately equal to the number of measurements. Hence, the cost will herein be quoted normalised by the length of $\boldsymbol{y}$.

It can be shown that the iteration,

$$\boldsymbol{x}_{i+1} = \boldsymbol{x}_i + [(1+\Gamma_i)\mathbf{S}_a^{-1} + \mathbf{K}_i^T \mathbf{S}_\epsilon^{-1}\mathbf{K}_i]^{-1}\{\mathbf{K}_i^T\mathbf{S}_\epsilon^{-1}[\boldsymbol{y} - F(\boldsymbol{x}_i, \boldsymbol{b})] - \mathbf{S}_a^{-1}(\boldsymbol{x}_i - \boldsymbol{x}_a)\}, \tag{3}$$

converges to the most probable state $\hat{\boldsymbol{x}}$, where the Jacobean $\mathbf{K}_i = \nabla_{\boldsymbol{x}_i} F(\boldsymbol{x}_i, \boldsymbol{b})$ and Γ_i is a scaling constant. General practice, outlined in Fig. 1, is that if the cost increases after an iteration, Γ_i is increased by a factor of ten. Otherwise, it is reduced by a factor of two. Evaluation ceases after:

- The cost function decreases by much less than the number of measurements;
- The cost decreased and the change in the state is much less than the predicted error,

  $$(\boldsymbol{x}_{i+1} - \boldsymbol{x}_i)_j \ll \sqrt{\mathbf{S}_{jj}} \quad \forall j,$$

  where the error covariance matrix of the solution $\mathbf{S} = (\mathbf{K}_i^T\mathbf{S}_\epsilon^{-1}\mathbf{K}_i + \mathbf{S}_a^{-1})^{-1}$.
- The step in state space,

  $$\{\mathbf{K}_i^T\mathbf{S}_\epsilon^{-1}[\boldsymbol{y} - F(\boldsymbol{x}_i, \boldsymbol{b})] - \mathbf{S}_a^{-1}(\boldsymbol{x}_i - \boldsymbol{x}_a)\}(\boldsymbol{x}_{i+1} - \boldsymbol{x}_i)^T,$$

  is much less than the length of the state vector;
- 30 iterations, which is considered a failure to converge.

The averaging kernel,

$$\mathbf{A} = \hat{\mathbf{S}}\hat{\mathbf{K}}^T\mathbf{S}_\epsilon^{-1}\hat{\mathbf{K}}, \tag{4}$$

describes the extent to which the true and a priori states each contribute to the solution as it can be shown that,

$$\hat{\boldsymbol{x}} = \mathbf{A}\boldsymbol{x} + (\mathbf{I} - \mathbf{A})\boldsymbol{x}_\mathrm{a} + \hat{\mathbf{S}}\hat{\mathbf{K}}^T\mathbf{S}_\epsilon^{-1}\boldsymbol{\epsilon}, \tag{5}$$

where a hat indicates the value after convergence. An ideal retrieval would have a kernel equal to the identity. In practice, the rows of **A** will be peaked functions showing how the information in one retrieved bin is derived from an average of the true values around it. The width of that peak is therefore a measure of the resolution of the retrieval.

2.2 Existing lidar analyses

The energy observed from a height R is expressed by the lidar equation (Measures, 1992),

$$E(R,\lambda) = \frac{E_\mathrm{L}\,C(R,\lambda)}{R^2}\bar{\beta}(R,\lambda)\exp\left[-\int_0^R \bar{\alpha}(R',\lambda_\mathrm{L}) + \bar{\alpha}(R',\lambda)\mathrm{d}R'\right], \tag{6}$$

where $\bar{\beta}(R,\lambda)$ is the coefficient for incident laser light, wavelength λ_L, to be backscattered at a wavelength λ; $\bar{\alpha}(R,\lambda)$ is the extinction coefficient; E_L is the energy of the laser pulse; and $C(R)$, known as the overlap function, describes the alignment and efficiency of the detection system. As both the extinction and backscatter are unknown, a single profile presents an underconstrained measurement.

The atmosphere is assumed to contain only two components such that,

$$\bar{\beta} = \beta + \beta^{(\mathrm{m})} \tag{7}$$

$$\bar{\alpha} = \alpha + \alpha^{(\mathrm{m})}, \tag{8}$$

where β, α denote backscattering and extinction by aerosols and $\beta^{(\mathrm{m})}$, $\alpha^{(\mathrm{m})}$ denote scattering by molecules, which is well-modelled by Rayleigh scattering.

The dominant return for any lidar is the elastic profile (where $\lambda = \lambda_L$), from which the backscatter is commonly derived by a technique known as onion peeling or the Fernald–Klett method (Klett, 1981; Fernald, 1984). A Raman lidar monitors a second channel containing the Raman scattering from a single species in the atmosphere, such that $\bar{\beta}$ becomes a known function of number density. Ansmann et al. (1992) outlined a means to invert Eq. (6) in such circumstances to derive the extinction and backscatter separately.

A few applications of non-linear regression to lidar have been published. A retrieval of ice water path and effective radius in cirrus clouds from coincident, space-borne lidar and radar measurements was developed in Delanoe and Hogan (2008), though its results were found to be highly dependant on the microphysical assumptions. Pounder et al. (2012) derived high-quality extinction retrievals from three simultaneous observations with different fields of view using a linearised model of the lidar equation that included multiple scattering while applying Twomey–Tikhonov smoothing rather than an a priori. Marchant et al. (2010) presented an original, if limited, linearised scheme that decomposed scattering over a basis of precomputed aerosols. This was expanded to a retrieval of effective radius in multiwavelength studies via a Kalman filter in Marchant et al. (2012).

A related method known as regularisation has also been applied to Raman lidar. The introduction of Veselovskii et al. (2002) provides a good review of early attempts and the methodology. Shcherbakov (2007) and Pornsawad et al. (2012) demonstrated that such methods return solely positive extinction and can produce more accurate products than the Ansmann method but require artificial smoothing within the retrieval, which generates significant errors where there are siginificant gradients. Evaluation also requires a set of basis functions to be defined, artificially imposing a structure onto the system.

It is preferable to impose the basis for smoothing solutions through an a priori covariance matrix derived from actual data and the physical processes driving the system, as facilitated by optimal estimation retrieval. The impact of these assumptions can be assessed through the averaging kernel, such that it is clear where the data are the dominant influence on the solution. Other techniques do not provide such a balance and, in fact, rarely discuss the choice of basis functions nor their impact on the solution.

2.3 Forward model

Lidars use photomultiplier tubes (PMTs) as their detector, which produce a current spike when struck by a photon. If the rate of photons is less than two per bin, noise can be very effectively removed by applying a discriminating threshold to the output, returning a count of the number of photons per bin. As count rates increase, multiple pulses are more likely to overlap and be counted only once, such that this mode becomes increasingly nonlinear (Müller, 1973). The most frequent correction for this (Whiteman et al., 1992) assumes that after any count, the detector will be "paralyzed" for a constant "dead time" τ_d such that the observed number of counts is,

$$\varphi_i = \frac{ME_i}{1 + \tau_\mathrm{d}\,\tau_\mathrm{b}^{-1} E_i}, \tag{9}$$

where M is the number of laser shots E is averaged over and τ_b is the duration of a bin (such that $R_i = \frac{1}{2} i c \tau_\mathrm{b}$). This will apply to both channels, though each may have a distinct value of τ_d.

For large count rates, it is also possible to operate the PMT in an analogue mode, which simply averages the output current during each range bin. This is linear over a large dynamic range but suffers additional noise from thermal excitations, variations in pulse height, electrical interference, and other effects. In such circumstances, φ is proportional to E.

To reduce the length of $\boldsymbol{x}$ and minimise the computational cost of the algorithm, the extinction and backscatter will be retrieved on a coarser axis than observed and then interpolated onto the instrument's vertical grid using the cubic spline method of Press et al. (1992). Arbitrary grids could be applied to each variable, but for simplicity a single

AMTD
6, 9297–9346, 2013

axis with even 33 m spacing will be used. Provided the grid size is smaller than the features to be resolved, its choice only impacts the computational cost.

Neglecting multiple scattering, the number of photons observed from range bin R_i will be,

$$E_i^{(\mathrm{L})} = E_\mathrm{L} \frac{C_i^{(\mathrm{L})}}{R_i^2} \left[\frac{\sigma_R^{(\mathrm{L})}}{\beta} N_i + \underset{r \to R_i}{\mathrm{spline}} [\tilde{\beta}] \right] \exp \left[-2 \left(\sigma_R^{(\mathrm{L})} \mathcal{N}_i + \underset{r \to R_i}{\mathrm{spline}} [\tilde{\chi}] \right) \right] + E_B^{(\mathrm{L})} \tag{10}$$

$$E_i^{(\mathrm{ra})} = E_\mathrm{L} \frac{C_i^{(\mathrm{ra})}}{R_i^2} N_i \exp \left[- \left(\sigma_R^{(\mathrm{L})} + \sigma_R^{(\mathrm{ra})} \right) \mathcal{N}_i - \left(1 + \frac{\lambda_\mathrm{L}}{\lambda_\mathrm{ra}} \right) \underset{r \to R_i}{\mathrm{spline}} [\tilde{\chi}] \right] + E_B^{(\mathrm{ra})}, \tag{11}$$

where $\mathcal{N}_i = \int_0^{R_i} N(R')\mathrm{d}R'$; a tilde represents a variable on the retrieved grid r; the aerosol optical thickness $\chi = \int_0^R \alpha(\lambda_\mathrm{L}, R')\mathrm{d}R'$; β and χ are evaluated at λ_L, though this dependence is dropped for brevity; and E_B is the background count rate which is estimated from observations as $R \to \infty$. The calibration function $C(R)$ is assumed known and is input into as a parameter.

The optical thickness is evaluated by the trapezium rule,

$$\tilde{\chi}_j = \tilde{\alpha}_0 r_0 + \frac{1}{2} \sum_{k=1}^{j} [\tilde{\alpha}_k + \tilde{\alpha}_{k-1}][r_k - r_{k-1}]. \tag{12}$$

Note that the extinction is assumed constant through the first bin, such that it acts as a boundary term rather than a physically meaningful value. This avoids various difficulties with observation very near the instrument.

Extinction and backscatter are both functions of N and so will be correlated. This should be identified within $\mathbf{S}_\mathrm{a}$ but is not be easily estimated. Further, the use of correlated variables will emphasise degenerate states of the forward model, which can slow the retrieval's convergence. This can be averted by retrieving the lidar ratio instead, which is independent of N,

AMTD
6, 9297–9346, 2013

$$\tilde{\chi}_j = \tilde{\beta}_0 \tilde{B}_0 r_0 + \frac{1}{2} \sum_{k=1}^{j} [\tilde{\beta}_k \tilde{B}_k + \tilde{\beta}_{k-1} \tilde{B}_{k-1}][r_k - r_{k-1}]. \tag{13}$$

All elements of $\boldsymbol{x}$ should be positive or the retrieval will explore unrealistic models. For the retrieval of β and α, this will be prevented by setting all negative values to zero after evaluating Eq. (3). For the retrieval of β and B, it was found preferable to instead retrieve $\ln \beta$ while enforcing a lower limit of unity on B.

The measurement and state vectors are then,

$$\boldsymbol{y} = \begin{pmatrix} \varphi_0^{(\mathrm{L})} \\ \varphi_1^{(\mathrm{L})} \\ \vdots \\ \varphi_{m-1}^{(\mathrm{L})} \\ \varphi_0^{(\mathrm{ra})} \\ \varphi_1^{(\mathrm{ra})} \\ \vdots \\ \varphi_{m-1}^{(\mathrm{ra})} \end{pmatrix} \quad \text{and} \quad \boldsymbol{x} = \begin{pmatrix} \tilde{\beta}_0 \\ \tilde{\beta}_1 \\ \vdots \\ \tilde{\beta}_{n-1} \\ \tilde{\alpha}_0 \\ \tilde{\alpha}_1 \\ \vdots \\ \tilde{\alpha}_{n-1} \end{pmatrix} \parallel \begin{pmatrix} \ln \tilde{\beta}_0 \\ \ln \tilde{\beta}_1 \\ \vdots \\ \ln \tilde{\beta}_{n-1} \\ \tilde{B}_0 \\ \tilde{B}_1 \\ \vdots \\ \tilde{B}_{n-1} \end{pmatrix}.$$

The first guess for $\boldsymbol{x}$ in the iteration Eq. (3) is taken as $\beta = 10^{-5}\,\mathrm{Mm}^{-1}\,\mathrm{sr}^{-1}$ and $B = 58\,\mathrm{sr}$. These values were chosen as they tend to reduce the number of iterations and their value does not affect the final result (if the retrieval converges).

One final note must be made of the treatment of measurement error (which is assumed uncorrelated), $\mathbf{S}_\epsilon$. The observed photon counts should be Poisson distributed, such that their variance is equal to their mean. This is widely used to justify approximating the variance of a lidar measurement with the measurement itself. This is not strictly valid as the measurement is only a single sample of a distribution. However, a lidar

AMTD
6, 9297–9346, 2013

sums profiles over several seconds or minutes of laser shots during data collection, giving no further measure of their variance.

The optimal estimation scheme requires an unbiased estimate of the variance. Using the measurement itself causes the retrieval to favour observations that coincidentally suffer large, positive noise as they are then presumed to be more precise. This effect is most pronounced at low signal levels and introduces a high bias into the retrieval. To alleviate this, the variance will be estimated from the application of a five-bin, sliding-window average to the data. The impact of this will not be explored in detail, though preliminary studies found that even minimal smoothing of the variance vastly reduced biases.

For further details, derivations, and justification of the forward model, please consult Chapt. 2 of Povey (2013).

2.4 A priori

Arguably the most important component of an optimal estimation scheme is its a priori. Ideally, the a priori would not greatly affect the retrieval, but in practice it constrains which states are deemed to be both physically possible and likely. In this problem, solutions should be reasonably smooth as aerosols are often well-mixed through the planetary boundary layer (PBL), but gradients shouldn't be completely excluded as layering does occur.

The exact composition and optical properties of aerosol are highly variable and climatologies (from which an a priori would be derived in most applications) rarely exist. Some generalised descriptions of representative aerosol types have been explored in the literature. The OPAC model (Optical Properties of Aerosol and Cloud, Hess et al., 1998) defines size distributions, refractive indices, and number densities for a variety of cloud and aerosol particles. These provide the necessary inputs for Mie codes (Grainger et al., 2004) to calculate the extinction and backscatter. Combinations of these based on expected and observed compositions then produce characteristic aerosol mixtures, such as marine or urban.

AMTD
6, 9297–9346, 2013

For the data to be considered, the continental type should be appropriate – comprising soot with soluble and insoluble aerosols. An ensemble of scattering properties was constructed by randomising the abundance of these components, using the OPAC model values as the mean of a Gaussian distribution with width estimated by 10 % of that mean (the exact value assumed was found to be unimportant). Aspherical particles produce an effectively identical distribution. The resulting distributions of β, α, and B are shown in Fig. 2. The a priori is based on qualitative fits to these, shown in blue when retrieving linearly and in red for a logarithmic retrieval. Though the logarithmic retrievals appear to give a better fit to the distributions, the retrieval of $\ln\beta$ and $\ln\alpha$ was found to be overly constrained. Though the lidar ratio is theoretically a better description of the state, its distribution is not symmetric and so not necessarily well-suited to optimal estimation. A relatively broad a priori distribution has been selected to compensate. These distributions demonstrate an approximately 95 % correlation between β and α, which is included in $\mathbf{S}_\mathrm{a}$ for the linear retrieval. Though its exact value appears to be unimportant, it would be desirable to obtain a more rigorous estimate.

The OPAC model states that the density of non-dust aerosols decreases exponentially with a scale height of 2 km. The prescribed values will therefore decrease similarly in $\boldsymbol{x}_\mathrm{a}$. Further, there will almost certainly be some vertical correlation of the measurements due to vertical mixing. The simple model of a Markov process proposed by (2.83) of Rodgers (2000) shall be used with correlations decaying exponentially with separation,

$$(\mathbf{S}_\mathrm{a})_{ij} = \sqrt{(\mathbf{S}_\mathrm{a})_{ii}(\mathbf{S}_\mathrm{a})_{jj}}\exp\left(-\frac{|r_i - r_j|}{H}\right), \tag{14}$$

where H is a scale height.

The scale height can be estimated by investigating the covariance of some measure of aerosol scattering. A convenient option is backscattersondes (NDACC, 2000), which measure the light backscattered from a zenon flashlamp approximately every 30 m during a balloon ascent (Rosen and Kjome, 1991; Rosen et al., 2000). Profiles over ten

AMTD
6, 9297–9346, 2013

years of observations at three sites have been used in Fig. 3 to produce a correlation matrix of backscatter ratio with height. Its rows decay roughly exponentially with height, which when fitted to Eq. (14) give $H = 1$–2 km in the free troposphere.

This will not necessarily apply within the PBL, which is only weakly coupled to the free troposphere (Oke, 1987). Several studies of the vertical distribution of aerosol within the PBL have been performed with tethered balloons, though the data could not be readily accessed. These generally find that aerosol concentrations are constant with height (Figs. 10–12, 4, and 2 of Ewell et al., 1989; Greenberg et al., 2009; Ferrero et al., 2010, respectively), but occasionally observe fine structure (Fig. 6 of Ferrero et al., 2011). Further, a myriad of literature covers observations of aerosol layers tens to hundreds of metres thick (e.g. Di Girolamo et al., 1999; Dacre et al., 2011) or variations within lofted aerosol features (e.g. Althausen et al., 2000; Huang et al., 2010).

The a priori covariance matrix should represent both the general tendency for aerosols to be well-mixed throughout the troposphere and the fine scale structure that occasionally occurs. The average position of the top of the PBL should be expressed by a significant decrease in correlation between areas above and below it. At the moment, there is insufficient information to quantify these effects with any degree of certainty. As such, a conservative estimate of $H = 100$ m is used, which will not make the best use of the available information but does not overconstrain the solution.

3 Simulations

Simulated data can be easily produced with the forward model, using the NOAA (1976) standard atmosphere. The PBL extinction profile is modelled by an error function (Steyn et al., 1999) multiplied by an exponential decay above the PBL. Aerosol and cloud layers are modelled by Gaussian peaks (Biavati, G., personal communication, 2011). An analytic model of the RACHEL instrument is used to generate the calibration function and detector nonlinearity (see Povey et al., 2012). Once simulated, Poisson noise is added to the profiles.

3.1 Sensitivity

The retrieval from six simulated profiles by both proposed configurations is shown in Fig. 4. The two configurations give equivalent results and successfully retrieve the simulated profile in cases (a–d). Cases (e) and (f) return large costs, such that it is obvious they have failed. In (e), an incorrect nonlinear correction causes an underestimation where the observed profile has maximal energy. The observation of a cloud in (f) is reasonable within the PBL but fails above that. The large scattering within the cloud is outside of the range prescribed by the a priori and, though it obtains a decent fit to the visible region of the cloud, vertical correlations cause incorrect retrieval beneath it. Successfully fitting cloud and aerosol observations simultaneously requires a more detailed forward model and a priori.

The lidar ratio profiles indicate that there is a decrease in the information content of the measurement above the PBL, where scattering (and therefore the magnitude of the return) is lower. The two configurations react differently to this. The lidar ratio configuration returns a smooth B profile that tends towards its a priori value above the PBL, as would be expected, while the extinction configuration gives a much noisier profile, indicating it is less constrained by the a priori.

A further six simulations containing small-scale fluctuations are presented in Fig. 5. The two configurations behave as before, with the lidar ratio mode returning a smoother profile but losing sensitivity above the PBL. The "layers" of cases (g) and (h) are correctly positioned by both modes, if slightly underestimated in magnitude. In case (i), the layers are not resolved (see Fig. 6) as the features occupied only one retrieval bin. Doubling the resolution gives equivalent performance to cases (g) and (h) but with slightly increased noise and significantly increased processing time. Cases (k) and (l) are more difficult retrievals as they present lower SNR. They are still consistent with the true profile but with greater errors.

Both configurations give a respectable fit to the extinction profile, though they do increasingly underestimate the magnitude of peaks as they become narrower. This de-

AMTD
6, 9297–9346, 2013

creased sensitivity is clear within the averaging kernels (Fig. 7). Though the backscatter kernels are virtually delta functions in the PBL, the extinction and lidar ratio kernels have widths of ~300 m (the effective resolution of those products). The kernels also illustrate the loss of sensitivity in the lidar ratio configuration above the PBL, with the magnitude of both kernels decreasing significantly. In cases (k) and (l), the sensitivity is also lower due to the reduced SNR. The extinction configuration maintains sensitivity throughout the profile, though its extinction kernels are skewed about their centre (which may derive from $E^{(ra)}$ measuring the integral of α, such that bins beneath a level contribute greater information content). Overall, the kernels indicate that the smoother profiles returned by the lidar ratio mode are due to a greater reliance on the a priori.

3.2 Error analysis

3.2.1 Retrieval error

The error covariance matrices for case (a) in both configurations are shown in Fig. 8. They confirm that the linear configuration makes the best use of the available information as that mode behaves identically within and above the PBL whilst the logarithmic configuration reverts to the a priori covariance in the free troposphere. Where there is information, the form of the covariance matrix has changed significantly from the a priori in both cases. Autocorrelation in the backscatter has decreased with regions near the surface being only 10 % correlated to adjacent bins. The extinction matrix, plots (d) and (i), show adjacent bins are correlated to ~60 % whilst other nearby bins are slightly anticorrelated. The intercorrelation of the variables has also evolved, with points above a level being anticorrelated and those below positively correlated. It will need to be confirmed if real data give similar results.

The diagonals of the covariances, plots (a) and (f), can be used to approximate the error on the products. These gives the bounds of Figs. 9 and 10. The lidar ratio a priori uncertainty is too small as it is not consistent with the simulated profile. Since that error is simply the a priori variance, this indicates that the a priori is overly constrictive. The

AMTD
6, 9297–9346, 2013

extinction retrieval is better, though it underestimates the error in the PBL. Both fail to appreciate the error caused by the improper dead time correction.

Those figures also compare the retrieval to the Ansmann method. For a fair comparison, the derivative is averaged over 300 m to be equivalent to the effective resolution of the retrieval. They are in good agreement in the PBL and the retrievals exhibit a lesser spread and error than the Ansmann solutions in the free troposphere. The Fernald–Klett method gives equivalent answers when given the correct lidar ratio.

3.2.2 Parameter error

In real retrievals, there will be some error in the model parameters $\boldsymbol{b}$. This additional uncertainty can be included in the retrieval by extending the measurement uncertainty to cover all sources of error,

$$\boldsymbol{\epsilon}_y = \boldsymbol{\epsilon} + \mathbf{K}_b(\boldsymbol{b} - \hat{\boldsymbol{b}}) + \boldsymbol{\Delta f}, \tag{15}$$

where $\mathbf{K}_b = \partial F / \partial \boldsymbol{b}$; $\hat{\boldsymbol{b}}$ is the best estimate of the true parameters $\boldsymbol{b}$; and the last term describes any inability of the forward model to describe the true state.

Concentrating on only the parameter error for now, this can be implemented by replacing all occurrences of $\mathbf{S}_\epsilon$ with,

$$\mathbf{S}_y = \mathbf{S}_\epsilon + \mathbf{K}_b \mathbf{S}_b \mathbf{K}_b^T. \tag{16}$$

This significantly increases the computing cost of the retrieval, as $\mathbf{S}_y$ must now be inverted in each iteration. A reasonable approximation is to only re-evaluate $\mathbf{S}_y$ after the last iteration. The full calculation is considered here.

The Ångstrom coefficient can vary quite significantly but is commonly accepted to lie in the range 0.6–1.4, such that an error of 0.4 is reasonable (Klett, 1985). Radiosondes measure pressure and temperature at a given height with an accuracy of 0.5 hPa, 2 K, and 60 m, from which an error in number density and $\chi^{(\mathrm{m})}$ of 0.5 % is expected (Kitchen,

AMTD
6, 9297–9346, 2013

1989). The height of the first observed bin, R_0, can be easily estimated to within 10 m. The standard deviation of the data used to estimate E_B can be easily derived.

The remaining parameters are estimated by some calibration procedure (e.g. Wandinger and Ansmann, 2002; Povey et al., 2012). For the purpose of demonstration, Fig. 11 shows the impact of each parameter on the total variance, assuming errors in C of 10 % and τ_d of 1 ns; these dominate the total. For the impact of uncertainty in C to be of a similar order to the measurement error, it must be known to within 2 % – an unrealistic expectation. However, these errors are unlikely to be correlated such that this term simply increases the total error.

The dead time is more troublesome for elastic measurements as it can introduce significant correlations within $\mathbf{S}_y$. For the system simulated with $\tau_d = 50$ ns, an error greater than 0.1 ns in its estimation significantly reduces the information content available and prevents the retrieval from converging. That is clearly an unrealistic expectation but is a fair representation of the impact that dead time has on the observations – an often overlooked source of error. Most laboratory standard systems will have much smaller dead times, which have a greater tolerance of around 1 ns.

The laser energy E_L behaves similarly to C but is considered separately as it can change significantly with time whilst the calibration function should be fairly consistent. For reasons particular to this study, the laser energy may not have always been accurately measured and so was retrieved as part of the state vector.

3.2.3 Further errors

The settings of the retrieval that have no bearing on the forward model should not affect $\hat{\boldsymbol{x}}$. The initial value of Γ_i alters the number of iterations required to converge as it drives the size of each step in state space. A value of 10^5 appears to be optimal in most cases and $\hat{\boldsymbol{x}}$ appears to be independent of that choice provided it is not too large or small. Similarly, convergence thresholds of 10^{-4} on change in cost or step and 10^{-1} on error were selected as the highest order for which $\hat{\boldsymbol{x}}$ is not affected by the choice. The minimum retrieved height does have a small effect on the retrieval in its first few bins,

AMTD
6, 9297–9346, 2013

Retrieval of backscatter and extinction from Raman lidar

A. C. Povey et al.

so $r_0 = 100$ m was chosen to concentrate these effects within a region where parameter errors will be large regardless.

Forward model error is defined in Sect. 3.2.3 of Rodgers (2000) as,

$$\mathbf{G}_y[\boldsymbol{f}(\boldsymbol{x},\boldsymbol{b},\boldsymbol{b}') - \boldsymbol{F}(\boldsymbol{x},\boldsymbol{b})], \tag{17}$$

where $\mathbf{G}_y = \partial\hat{\boldsymbol{x}}/\partial\boldsymbol{y}$, the sensitivity of the retrieved state to the measurement, and $\boldsymbol{f}$ is the exact, true profile including any processes the forward model $\boldsymbol{F}$ may not describe. This systematic error is generally difficult to estimate as, if $\boldsymbol{f}$ were known, it would most likely be used as the forward model instead.

There are some processes that are clearly not included within the current forward model. Multiple scattering has been neglected as it is mostly important for lidars with a wide footprint, such as space-based system, or for observations within clouds, where this algorithm is already known to perform poorly for other reasons. Though appropriate numerical models of multiple scattering exist (Eloranta, 1998), this is left as an area for future work if retrievals within clouds are desired.

There is a small difference between the bin-averaged backscatter that is sampled and the true backscatter defined by Mie theory, for which the error can be evaluated with Eq. (17). It is greatest in the entrainment layer (or at any other sharp gradient), being at most 1 % of the total error.

The models of the calibration function and detector nonlinearity are idealised versions of the truth. A rough estimate of these contributions can be produced by considering alternative models, such as Donovan et al. (1993). For case (e), these are over 100 times larger than the other errors, again demonstrating that great care must be taken with the dead time correction. Measurements in the linear observation regime are negligibly affected by the choice of nonlinear correction.

None of these errors describe the discrepancies shown in the free troposphere in Fig. 9 as that is dominated by the a priori uncertainty. In regions where the data are the dominant contribution to the retrieval (i.e. where the area of the averaging kernel is near unity), increasing the a priori variance does not affect the retrieved profiles.

AMTD
6, 9297–9346, 2013

Where it is important, the error estimate should clearly be greater to better represent the uncertainty. Hence, the a priori uncertainty in B will be increased to 40 sr. This is effectively a uniform distribution in Fig. 2.

4 Application

4.1 Individual profiles

The retrieval is now applied to observations by the Chilbolton Ultraviolet Raman lidar (CUV) (Agnew, 2003; Agnew and Wrench, 2006–2010), which is stationed at the Natural Environment Research Council (NERC) Chilbolton Facility for Atmospheric and Radio Research (CFARR, 51.1445° N, 1.4270° W, 84 m a.s.l., STFC, 2011). It uses a 355 nm Nd:YAG laser at 350 mJ and 50 Hz for water vapour profiling through the daytime boundary layer on a case-study basis, implementing both photon-counting and analogue data collection. Its observations can be directly compared to those of a Leosphere EZ lidar operated continuously at the same site, which provides depolarization profiles instead of Raman observations. Radiosonde launches are available twice daily from Larkhill, 30 km northwest (UK Met Office, 2011).

Six profiles were selected from March 2010 for which the instrument's calibration has been thoroughly investigated using the techniques of Povey et al. (2012). Figure 12 compares the retrieved profiles to those given by the Fernald–Klett and Ansmann methods. A clear atmosphere is assumed between 4–5 km using a constant B to give an optical thickness consistent with sunphotometer observations and the derivative is evaluated over 150 m. In the PBL, the retrieved backscatter is very similar to that given by the Ansmann ratio and an independent measurement by the EZ lidar. As the SNR decreases, the retrieval tends towards the Fernald–Klett solution. This is a proper response for the retrieval, giving answers similar to existing methods but tending from a two to one-channel retrieval as the available information decreases. This is also expressed in the averaging kernels, which widen from 30 to 100 m.

AMTD
6, 9297–9346, 2013

Retrieval of backscatter and extinction from Raman lidar

A. C. Povey et al.

The retrieved extinction is consistent with the Ansmann solution but gives a much smoother solution. The averaging kernels confirm that there is little information available in the free troposphere but also show that the resolution in the PBL is better than that observed in simulations: 100 m. A tendency to find $\alpha = 0$ at the top of the PBL is due to the number density profile. The radiosonde that morning recorded a step decrease in pressure at the top of the PBL, but as that is a low-resolution measurement, linear interpolation overestimates N there. A standard atmosphere does no better. Due to factors such as these, the inclusion of parameter errors significantly reduces the information content in the free troposphere. This can ocassionally produce unconstrained solutions due to the relatively weak a priori (not shown) but this does not significantly alter the result within the PBL. The errors, shown in Fig. 13, are similar to those of Fig. 8 but:

- Larger background levels (being daytime observations) produce large correlations at the top of the profile. The two modes respond differently to this, with the logarithmic configuration reverting to the a priori covariance at the top of the PBL (as observed in simulations) and the linear configuration tending towards complete correlation (representing a more systematic error).

- The intercorrelation of β and α is different. Bins above a point are still negatively correlated, but those below are more weakly correlated. The exact reason for this is not clear.

4.2 Extended periods

Eleven hours of photon counting observations were processed from 2 March 2010. Figure 14 plots retrievals with an error less than 20 % or 30 sr (β and B, respectively). Row (a) shows the application of the Ansmann method, where the data were averaged over 30 m to give a similar resolution to the retrieval. Row (b) is the linear retrieval and (c) the logarithmic. The three backscatter fields are qualitatively similar before 14:00 GMT and after 18:00 GMT. Between these times, the measurement of laser energy has diverged

AMTD
6, 9297–9346, 2013

increasingly from reality. As the retrieval has no knowledge of that, it retrieves smaller backscatter to compensate. The Ansmann method is not affected as it considers a ratio of channels. The difference between the Ansmann solution and the retrieval is effectively a constant factor of the failure in the calibration, with the results otherwise being consistent. For example, both methods observe larger β in updrafts than downdrafts (where vertical wind was observed by a Doppler lidar).

The retrievals are consistent in their estimates of the lidar ratio and are no worse than the Ansmann method, which is greatly affected by overlap when estimating α. The aerosol layer near 1 km at 10:00 GMT gives a lidar ratio of around 30 sr. This is a residual layer lying above a developing mixed layer where lidar ratios are larger (around 50 sr). The low lidar ratio indicates large, likely spherical, particles which are reasonable for an aged residual layer. The results are better in the evening, observing a peak B of 70 sr over a background of 50 sr, indicating the appearance of smaller particles. By this time, convective mixing has collapsed into a persistent updraft so the increase in depolarization ratio could indicate that newer, non-spherical particles are being lofted from the surface or are advected over the site. Advected aerosol is more likely considering the brevity of the peak.

Figure 15 compares the retrieved χ_∞ during that day to AERONET measurements (Woodhouse and Agnew, 2010–2011). Their agreement is reasonable if not impressive. The retrieval tends to return larger χ than observed by AERONET, though it also contains substantial variability that the latter does not. This is likely due to the inaccurate measurement of laser energy, though this is under investigation. A calibration performed at 10:00 GMT was used throughout this day and that is the only AERONET measurement that was in any way input into the retrieval – the remainder are independent. Regardless, the retrieved values are equivalent to those given by the Ansmann algorithm, indicating that the retrieval is correct for the parameters it has been given. It is the calibration of the system, not the method of retrieval, producing the poor comparison.

AMTD
6, 9297–9346, 2013

4.3 Eyjafjallajökull ash

The eruptions of the Eyjafjallajökull volcano in Southern Iceland during April and May of 2010 produced the single most significant volcanic ash event over Northern Europe in the age of aviation. The closure of airspace cancelled around 100 000 flights, inconveniencing millions of travellers across the globe and resulting in massive losses for airlines and related industries. Owing to the density of personnel and instrumentation within the reach of this plume, it has become one of the most studied atmospheric events in history. The introduction of Johnson et al. (2012) provides a reasonable overview of the literature published to date and more will certainly be published over the years to come.

The CUV was operated, in addition to routine measurements, on 19 April to observe ash within the boundary layer. The optimal estimation retrieval (in extinction mode) was applied to these observations, shown in Fig. 16. Plot (a) presents the depolarization ratio observed by the EZ lidar while plots (c–d) show the retrieved backscatter and lidar ratio with errors outlined in plots (e–f). Ash particles have a large depolarization due to their asphericity and these measurements indicate the presence of a 400 m thick ash layer within the PBL, though the observed value of 0.1 is smaller than that expected for mineral dusts (0.35–0.37, Ansmann et al., 2011). It exhibits a low backscatter ($<$ 10 $\mathrm{Mm^{-1}\,sr^{-1}}$) and lidar ratio (20–30 sr) compared to the remainder of the scene. These are well outside the range of 50–82 sr reported in the literature for similar ash in the free troposphere (Ansmann et al., 2010; Marenco and Hogan, 2011; Hervo et al., 2012). Combined with a smaller depolarization ratio, the retrieval indicates that the properties of the ash have changed significantly after 12–24 h within the PBL. The decreased B implies a growth of the particles, though this occurs without the influence of water as Raman observations indicate that the humidity is half its ambient value.

A mixed layer forms beneath the aerosol (see the vertical velocity in plot b). There, B = 50–80 sr with minimal depolarization, which is broadly consistent with urban aerosols (Müller et al., 2007). Backscatter is fairly homogeneous throughout the

AMTD
6, 9297–9346, 2013

layer except during a period of updrafts around 13:00 GMT when β decreases from 10 to 6 $\mathrm{Mm^{-1}\,sr^{-1}}$. The absence of a similar change elsewhere in the PBL gives some confidence that this is a real variation rather than a calibration artefact.

A more weakly depolarizing aerosol resides in a poorly-mixed residual layer above the ash layer. It persists until 14:00 GMT when they mix. Backscatter and lidar ratios are large at the top of this layer and decrease with height. This could be simple stratification within a poorly-mixed layer or smaller particles may have concentrated at the top of the layer whilst larger particles have begun to settle, though it does not seem that sufficient time has passed to produce so large a gradient.

Finally, a thin layer of aerosol is present above the PBL (labelled in plot c). The EZ lidar did not resolve this, so no measure of the depolarization is available. Expressing lidar ratios of 40–60 sr with low β, the layer is consistent with aerosol typically observed at CFARR and there is no reason to label it as ash.

Figure 18 presents the distribution of retrieved extinction and backscatter for all points with a depolarization ratio measured to better than 100 %. Lines of constant B are added for reference. Points likely to contain ash are shown in the left plot by filtering for depolarizations greater than 0.03. The residual layer appears as a concentration of points around $\beta = 10\,\mathrm{Mm^{-1}\,sr^{-1}}$ and $B \simeq 40$ sr. The mixed layer appears in the right plot as a more continuous distribution between $B = 40$ and 60 sr. The failure of the retrieval near the surface is evident in a vertical line of points at $\beta = 8\,\mathrm{Mm^{-1}\,sr^{-1}}$. In the free troposphere, $\beta < 1\,\mathrm{Mm^{-1}\,sr^{-1}}$, where poorly constrained retrievals produce a broad distribution in both plots. There are very few observations of the thin ash layer, but their presence is evident in observations near $B \simeq 20$ sr in the left plot not expressed on the right.

AMTD
6, 9297–9346, 2013

5 Conclusions

An optimal estimation retrieval scheme for aerosol scattering properties from Raman lidar observations was proposed, using the lidar equations as a simple forward model. The a priori state and covariance matrix were based on the properties of aerosol outlined in the OPAC model. Scattering was assumed to be vertically correlated between bins, decaying exponentially over a scale height of 100 m. This is smaller than observed by balloon-borne measurements but ensures that the PBL and free troposphere are not coupled.

The state of the atmosphere can be described at each height by the aerosol backscatter and either the extinction or lidar ratio. These possibilities were assessed by considering their ability to process simulated data. The lidar ratio configuration was found to lose sensitivity in the free troposphere, relying excessively upon its a priori assumptions, as shown by the disappearance of the averaging kernel. If extinction is retrieved instead, it and backscatter should be retrieved linearly with a correlation assumed between them (95 % here, though more investigation of this value is necessary). This configuration maintains sensitivity throughout the profile.

In the analysis of simulated and real data, the proposed retrieval is consistent with existing analyses. In addition, it returns a more rigorous estimate of the uncertainties. Backscatter was always retrieved at the finest resolution allowed (mostly 33 m, but this remains true at the instrumental limit < 10 m) and with an uncertainty between 2 % in the most ideal circumstances and 20 % in the least. Extinction and the lidar ratio are less well constrained, expressing resolutions of 300–500 m in simulations and 0.1–1 km with real data. Importantly, these are different from the scale of vertical correlations assumed a priori and increase as SNR decreases. The retrieval has selected the most suitable resolution independently, unlike the smoothing filters used in most studies. The uncertainty in extinction retrieved from real data is relatively large (> 15 %) but that is in part due to the short time scales evaluated (one minute in Figs. 14 and 16). The integration time can be increased to reduce these errors to any desired level (at least

AMTD
6, 9297–9346, 2013
Retrieval of backscatter and extinction from Raman lidar
A. C. Povey et al.

until atmospheric variability begins to dominate). Regardless, errors are comparable to, if not smaller than, fair estimates of the error resulting from the standard Raman lidar technique of Ansmann et al. (1992) applied to the same data.

The magnitude of the uncertainty was shown to be dominated by the calibration of the instrument – primarily the offset of its vertical axis, the nonlinear response of its detectors, and the calibration function. Ideally, all of these would be determined with dedicated laboratory measurements, especially the offset and nonlinearity which should change very little over time. These sources of error are not often discussed and the relative ease with which they can be included and studied within optimal estimation is one of its many strengths.

The retrieval was then applied to several hours of observation on 19 April 2010 of ash from the Eyjafjallajökull eruption. A highly depolarizing ash layer was observed with a lidar ratio of 20–30 sr, much lower than observed in the free troposphere by previous studies and potentially indicating a growth of the particles after 12–24 h within the planetary boundary layer. More dispersed ash within a residual layer exhibited a backscatter of 10 $\mathrm{Mm^{-1}\,sr^{-1}}$ and lidar ratio of 40 sr.

Acknowledgement. This work was supported by a NERC studentship in association with Hovemere, Ltd.

References

Agnew, J. L.: Lidar and radar tropospheric profiling at Chilbolton Observatory, in: Sixth International Symposium on Tropospheric Profiling: Needs and Technologies, Leipzig, Germany, 14–20 September 2003, 151–153, 2003. 9315

Agnew, J. and Wrench, C.: Chilbolton UV Raman Lidar Raw Data, STFC Chilbolton Observatory, Rutherford Appleton Laboratory, available at: http://badc.nerc.ac.uk/view/badc.nerc.ac.uk__ATOM__dataent_chobs, 2006–2010. 9315

Althausen, D., Müller, D., Ansmann, A., Wandinger, U., Hube, H., Clauder, E., and Zörner, S.: Scanning 6-wavelength 11-channel aerosol lidar, J. Atmos. Ocean. Tech., 17, 1469–1482, doi:10.1175/1520-0426(2000)017<1469:swcal>2.0.co;2, 2000. 9309

Discussion Paper | Discussion Paper | Discussion Paper | Discussion Paper |

AMTD

6, 9297–9346, 2013

Retrieval of backscatter and extinction from Raman lidar

A. C. Povey et al.

Ansmann, A., Wandinger, U., Riebesell, M., Weitkamp, C., and Michaelis, W.: Independent measurement of extinction and backscatter profiles in cirrus clouds by using a combined Raman elastic-backscatter lidar, Appl. Optics, 31, 7113–7131, doi:10.1364/AO.31.007113, 1992. 9303, 9321

Ansmann, A., Tesche, M., Gross, S., Freudenthaler, V., Seifert, P., Hiebsch, A., Schmidt, J., Wandinger, U., Mattis, I., Müller, D., and Wiegner, M.: The 16 April 2010 major volcanic ash plume over Central Europe: EARLINET lidar and AERONET photometer observations at Leipzig and Munich, Germany, Geophys. Res. Lett., 37, L13810, doi:10.1029/2010gl043809, 2010. 9318

Ansmann, A., Tesche, M., Seifert, P., Gross, S., Freudenthaler, V., Apituley, A., Wilson, K. M., Serikov, I., Linné, H., Heinold, B., Hiebsch, A., Schnell, F., Schmidt, J., Mattis, I., Wandinger, U., and Wiegner, M.: Ash and fine-mode particle mass profiles from EARLINET-AERONET observations over Central Europe after the eruptions of the Eyjafjallajökull volcano in 2010, J. Geophys. Res.-Atmos., 116, D00U02, doi:10.1029/2010jd015567, 2011. 9318

Colbeck, I.: Physical and Chemical Properties of Aerosols, 1st edn., Blackie Academic and Professional, London, 1998. 9298

Dacre, H. F., Grant, A. L. M., Hogan, R. J., Belcher, S. E., Thomson, D. J., Devenish, B. J., Marenco, F., Hort, M. C., Haywood, J. M., Ansmann, A., Mattis, I., and Clarisse, L.: Evaluating the structure and magnitude of the ash plume during the initial phase of the 2010 Eyjafjallajökull eruption using lidar observations and NAME simulations, J. Geophys. Res.-Atmos., 116, D00U03, doi:10.1029/2011jd015608, 2011. 9309

Delanoe, J. and Hogan, R. J.: A variational scheme for retrieving ice cloud properties from combined radar, lidar, and infrared radiometer, J. Geophys. Res.-Atmos., 113, D07204, doi:10.1029/2007jd009000, 2008. 9303

Di Girolamo, P., Ambrico, P. F., Amodeo, A., Boselli, A., Pappalardo, G., and Spinelli, N.: Aerosol observations by lidar in the nocturnal boundary layer, Appl. Optics, 38, 4585–4595, doi:10.1364/AO.38.004585, 1999. 9309

Donovan, D. P., Whiteway, J. A., and Carswell, A. I.: Correction for nonlinear photon-counting effects in lidar systems, Appl. Optics, 32, 6742–6753, doi:10.1364/AO.32.006742, 1993. 9314

Eloranta, E. W.: Practical model for the calculation of multiply scattered lidar returns, Appl. Optics, 37, 2464–2472, doi:10.1364/AO.37.002464, 1998. 9314

AMTD

6, 9297–9346, 2013

Retrieval of backscatter and extinction from Raman lidar

A. C. Povey et al.

Title Page
Abstract | Introduction
Conclusions | References
Tables | Figures
◀| |▶
◀ ▶
Back | Close
Full Screen / Esc
Printer-friendly Version
Interactive Discussion

Ewell, D. M., Flocchini, R. G., Myrup, L. O., and Cahill, T. A.: Aerosol transport in the Southern Sierra-Nevada, J. Appl. Meteorol., 28, 112–125, doi:10.1175/1520-0450(1989)028<0112:atitss>2.0.co;2, 1989. 9309

Fernald, F. G.: Analysis of atmospheric lidar observations – some comments, Appl. Optics, 23, 652–653, doi:10.1364/AO.23.000652, 1984. 9303

Ferrero, L., Perrone, M. G., Petraccone, S., Sangiorgi, G., Ferrini, B. S., Lo Porto, C., Lazzati, Z., Cocchi, D., Bruno, F., Greco, F., Riccio, A., and Bolzacchini, E.: Vertically-resolved particle size distribution within and above the mixing layer over the Milan metropolitan area, Atmos. Chem. Phys., 10, 3915–3932, doi:10.5194/acp-10-3915-2010, 2010. 9309

Ferrero, L., Mocnik, G., Ferrini, B. S., Perrone, M. G., Sangiorgi, G., and Bolzacchini, E.: Vertical profiles of aerosol absorption coefficient from micro-Aethalometer data and Mie calculation over Milan, Sci. Total Environ., 409, 2824–2837, doi:10.1016/j.scitotenv.2011.04.022, 2011. 9309

Fugii, T. and Fukuchi, T.: Laser Remote Sensing, Taylor and Francis, Boca Raton, FL, 2005. 9299

Grainger, R. G., Lucas, J., Thomas, G. E., and Ewen, G. B. L.: Calculation of Mie derivatives, Appl. Optics, 43, 5386–5393, doi:10.1364/ao.43.005386, codes may be found at: http://www-atm.physics.ox.ac.uk/code/mie/ (last access: 21 June 2013), 2004. 9307

Grant, J., Grainger, R. G., Lawrence, B. N., Fraser, G. J., von Biel, H. A., Heuff, D. N., and Plank, G. E.: Retrieval of mesospheric electron densities using an optimal estimation inverse method, J. Atmos. Sol.-Terr. Phy., 66, 381–392, doi:10.1016/j.jastp.2003.12.006, 2004. 9299

Greenberg, J. R., Guenther, A. B., and Turnipseed, A.: Tethered balloon-based soundings of ozone, aerosols, and solar radiation near Mexico City during MIRAGE-MEX, Atmos. Environ., 43, 2672–2677, doi:10.1016/j.atmosenv.2009.02.019, 2009. 9309

Guldner, J. and Spankuch, D.: Remote sensing of the thermodynamic state of the atmospheric boundary layer by ground-based microwave radiometry, J. Atmos. Ocean. Tech., 18, 925–933, doi:10.1175/1520-0426(2001)018<0925:rsotts>2.0.co;2, 2001. 9299

Haywood, J. M. and Shine, K. P.: The effect of anthropogenic sulfate and soot aerosol on the clear-sky planetary radiation budget, Geophys. Res. Lett., 22, 603–606, doi:10.1029/95gl00075, 1995. 9298

Hervo, M., Quennehen, B., Kristiansen, N. I., Boulon, J., Stohl, A., Fréville, P., Pichon, J.-M., Picard, D., Labazuy, P., Gouhier, M., Roger, J.-C., Colomb, A., Schwarzenboeck, A., and Sellegri, K.: Physical and optical properties of 2010 Eyjafjallajökull volcanic eruption aerosol:

ground-based, Lidar and airborne measurements in France, Atmos. Chem. Phys., 12, 1721–1736, doi:10.5194/acp-12-1721-2012, 2012. 9318

Hess, M., Koepke, P., and Schult, I.: Optical properties of aerosols and clouds: the software package OPAC, B. Am. Meteorol. Soc., 79, 831–844, doi:10.1175/1520-0477(1998)079<0831:opoaac>2.0.co;2, 1998. 9307

Huang, Z. W., Huang, J. P., Bi, J. R., Wang, G. Y., Wang, W. C., Fu, Q. A., Li, Z. Q., Tsay, S. C., and Shi, J. S.: Dust aerosol vertical structure measurements using three MPL lidars during 2008 China-US joint dust field experiment, J. Geophys. Res.-Atmos., 115, D00K15, doi:10.1029/2009jd013273, 2010. 9309

Intergovernmental Panel on Climate Change (IPCC), Solomon, S., Qin, D., Manning, M., Chen, Z., Marquis, M., Averyt, K. B., Tignor, M., and Miller, H. L.: Climate Change 2007: The Physical Basis of Climate Change, Contribution of Working Group I to the Fourth Assessment Report of the Intergovernmental Panel on Climate Change, Cambridge University Press, New York, 2007. 9299

Johnson, B., Turnbull, K., Brown, P., Burgess, R., Dorsey, J., Baran, A. J., Webster, H., Haywood, J., Cotton, R., Ulanowski, Z., Hesse, E., Woolley, A., and Rosenberg, P.: In situ observations of volcanic ash clouds from the FAAM aircraft during the eruption of Eyjafjallajökull in 2010, J. Geophys. Res.-Atmos., 117, D00U24, doi:10.1029/2011jd016760, 2012. 9318

Kitchen, M.: Representativeness errors for radiosonde observations, Q. J. Roy. Meteor. Soc., 115, 673–700, doi:10.1256/smsqj.48712, 1989. 9312

Klett, J. D.: Stable analytical inversion solution for processing lidar returns, Appl. Optics, 20, 211–220, doi:10.1364/AO.20.000211, 1981. 9303

Klett, J. D.: Lidar inversion with variable backscatter extinction ratios, Appl. Optics, 24, 1638–1643, doi:10.1364/AO.24.001638, 1985. 9312

Li, W., Stamnes, K., Spurr, R., and Stamnes, J.: Simultaneous retrieval of aerosol and ocean properties by optimal estimation: SeaWiFS case studies for the Santa Barbara Channel, Int. J. Remote Sens., 29, 5689–5698, doi:10.1080/01431160802007632, 2008. 9299

Lohmann, U. and Feichter, J.: Global indirect aerosol effects: a review, Atmos. Chem. Phys., 5, 715–737, doi:10.5194/acp-5-715-2005, 2005. 9298

Marchant, C. C., Moon, T. K., and Gunther, J. H.: An iterative least square approach to elastic-lidar retrievals for well-characterized aerosols, IEEE T. Geosci. Remote, 48, 2430–2444, doi:10.1109/tgrs.2009.2038903, 2010. 9303

AMTD

6, 9297–9346, 2013

Retrieval of backscatter and extinction from Raman lidar

A. C. Povey et al.

Marchant, C. C., Wojcik, M. D., and Bradford, W. J.: Estimation of aerosol effective radius by multiwavelength elastic lidar, IEEE T. Geosci. Remote, 50, 645–660, doi:10.1109/tgrs.2011.2160725, 2012. 9303

Marenco, F. and Hogan, R. J.: Determining the contribution of volcanic ash and boundary layer aerosol in backscatter lidar returns: a three-component atmosphere approach, J. Geophys. Res.-Atmos., 116, D00U06, doi:10.1029/2010jd015415, 2011. 9318

Marks, C. J. and Rodgers, C. D.: A retrieval method for atmospheric composition from limb emission measurements, J. Geophys. Res.-Atmos., 98, 14939–14953, doi:10.1029/93jd01195, 1993. 9299

Measures, R. M.: Lidar Remote Sensing: Fundamentals and Applications, 2nd edn., Krieger Publishing Company, Malabar, FL, 1992. 9302

Müller, D., Wandinger, U., and Ansmann, A.: Microphysical particle parameters from extinction and backscatter lidar data by inversion with regularization: theory, Appl. Optics, 38, 2346–2357, doi:10.1364/AO.38.002346, 1999. 9299

Müller, D., Ansmann, A., Mattis, I., Tesche, M., Wandinger, U., Althausen, D., and Pisani, G.: Aerosol-type-dependent lidar ratios observed with Raman lidar, J. Geophys. Res.-Atmos., 112, D16202, doi:10.1029/2006jd008292, 2007. 9318

Müller, J. W.: Dead-time problems, Nucl. Instrum. Methods, 112, 47–57, doi:10.1016/0029-554x(73)90773-8, 1973. 9304

National Oceanic and Atmospheric Administration (NOAA): US Standard Atmosphere, Tech. Rep. NOAA Doc. S/T 76-1562, US Government Printing Office, Washington, D.C., 1976. 9309

Network for the Detection of Atmospheric Composition Change (NDACC) (Rosen, J.): Backscattersonde data (Laramie, WY; Lauder, New Zealand; Thule, Greenland), Supported by NSF grants OPP-9423285, ATM-9500186, 1989–2000. 9308

Oke, T. R.: Boundary Layer Climates, 2nd edn., Cambridge University Press, London, UK, 1987. 9309

Pappalardo, G., Amodeo, A., Mona, L., and Pandolfi, M.: Systematic measurements of the aerosol extinction-to-backscatter ratio, in: Lidar Remote Sensing for Industry and Environmental Monitoring V, vol. 5653, edited by: Singh, U. N. and Mizutani, K., SPIE, Bellingham, WA, 77–87, doi:10.1117/12.578809, 2005. 9299

Pornsawad, P., D'Amico, G., Böckmann, C., Amodeo, A., and Pappalardo, G.: Retrieval of aerosol extinction coefficient profiles from Raman lidar data by inversion method, Appl. Optics, 51, 2035–2044, doi:10.1364/AO.51.002035, 2012. 9303

Pounder, N. L., Hogan, R. J., Várnai, T., Battaglia, A., and Cahalan, R. F.: A variational method to retrieve the extinction profile in liquid clouds using multiple-field-of-view lidar, J. Appl. Meteorol. Clim., 51, 350–365, doi:10.1175/jamc-d-10-05007.1, 2012. 9303

Povey, A.: The application of optimal estimation retrieval to lidar observations, Ph.D. thesis, University of Oxford, Oxford, UK, 2013. 9307

Povey, A. C., Grainger, R. G., Peters, D. M., Agnew, J. L., and Rees, D.: Estimation of a lidar's overlap function and its calibration by nonlinear regression, Appl. Optics, 51, 5130–5143, doi:10.1364/AO.51.005130, 2012. 9309, 9313, 9315

Press, W. H., Vetterling, W. T., Teukolsky, S. A., and Flannery, B. P.: Numerical Recipes in C: The Art of Scientific Computing, 2nd edn., Cambridge University Press, New Delhi, India, 1992. 9304

Rodgers, C. D.: Inverse Methods for Atmospheric Sounding: Theory and Practice, 2nd edn., Series on Atmospheric, Oceanic, and Planetary Physics, vol. 2, World Scientific, Singapore, 2000. 9300, 9308, 9314

Rosen, J. M. and Kjome, N. T.: Backscattersonde – a new instrument for atmospheric aerosol research, Appl. Optics, 30, 1552–1561, doi:10.1364/AO.30.001552, 1991. 9308

Rosen, J., Young, S., Laby, J., Kjome, N., and Gras, J.: Springtime aerosol layers in the free troposphere over Australia: Mildura Aerosol Tropospheric Experiment (MATE 98), J. Geophys. Res.-Atmos., 105, 17833–17842, doi:10.1029/2000jd900208, 2000. 9308

Science and Technology Facilities Council (STFC) (Wrench, C. L.): Chilbolton Facility for Atmospheric and Radio Research (CFARR) data, available from NCAS British Atmospheric Data Centre at: http://badc.nerc.ac.uk/view/badc.nerc.ac.uk__ATOM__dataent_chobs (last access: 9 November 2010), 2006–2011. 9315

Shcherbakov, V.: Regularized algorithm for Raman lidar data processing, Appl. Optics, 46, 4879–4889, doi:10.1364/AO.46.004879, 2007. 9303

Steyn, D. G., Baldi, M., and Hoff, R. M.: The detection of mixed layer depth and entrainment zone thickness from lidar backscatter profiles, J. Atmos. Ocean. Tech., 16, 953–959, doi:10.1175/1520-0426(1999)016<0953:TDOMLD>2.0.CO;2, 1999. 9309

Sugimoto, N., Matsui, I., Shimizu, A., Nishizawa, T., Hara, Y., Chenbo, X., Uno, I., Yumimoto, K., Zifa, W., and Soon-Chang, Y.: Lidar network observations of tropospheric aerosols, Proc. SPIE, 7153, 71530A, doi:10.1117/12.806540, 2008. 9299

UK Meteorological Office (Parton, G.): Met Office Global Radiosonde Data, available from the NCAS British Atmospheric Data Centre at: http://badc.nerc.ac.uk/view/badc.nerc.ac.uk__ATOM__dataent_GLOBRADS (last access: 9 February 2011), 2006–2011. 9315

Vaughan, M., Young, S., Winker, D., Powell, K., Omar, A., Liu, Z. Y., Hu, Y. X., and Hostetler, C.: Fully automated analysis of space-based lidar data: an overview of the CALIPSO retrieval algorithms and data products, BBA Lib., 5575, 16–30, doi:10.1117/12.572024, 2004. 9299

Veselovskii, I., Kolgotin, A., Griaznov, V., Müller, D., Wandinger, U., and Whiteman, D. N.: Inversion with regularization for the retrieval of tropospheric aerosol parameters from multiwavelength lidar sounding, Appl. Optics, 41, 3685–3699, doi:10.1364/ao.41.003685, 2002. 9303

Wandinger, U. and Ansmann, A.: Experimental determination of the lidar overlap profile with Raman lidar, Appl. Optics, 41, 511–514, doi:10.1364/AO.41.000511, 2002. 9313

Watts, P. D., Bennartz, R., and Fell, F.: Retrieval of two-layer cloud properties from multispectral observations using optimal estimation, J. Geophys. Res.-Atmos., 116, D16203, doi:10.1029/2011jd015883, 2011. 9299

Welton, E. J., Campbell, J. R., Spinhirne, J. D., and Scott, V. S.: Global monitoring of clouds and aerosols using a network of micro-pulse lidar systems, in: Conference on Lidar Remote Sensing for Industry and Environment Monitoring, Vol. 4153, Sendai, Japan, 9–12 October 2000, 151–158, doi:10.1117/12.417040, 2001. 9299

Whiteman, D. N., Melfi, S. H., and Ferrare, R. A.: Raman lidar system for the measurement of water-vapor and aerosols in the Earth's atmosphere, Appl. Optics, 31, 3068–3082, doi:10.1364/AO.31.003068, 1992. 9304

Woodhouse, I. and Agnew, J.: Chilbolton AERONET Level 2.0 real time data, available from NASA GSFC at: http://aeronet.gsfc.nasa.gov (last access: 31 March 2013), 2010–2011. 9317

AMTD

6, 9297–9346, 2013

Retrieval of backscatter and extinction from Raman lidar

A. C. Povey et al.

AMTD
6, 9297–9346, 2013

Retrieval of backscatter and extinction from Raman lidar

A. C. Povey et al.

Table 1. A priori values and uncertainties, as shown in Fig. 2.

		β	α	B
Linear	Mean	4×10^{-6}	2×10^{-4}	58
	SD	3×10^{-6}	2×10^{-4}	7
Log	Mean	−12.4	−8.2	–
	SD	0.4	0.5	–

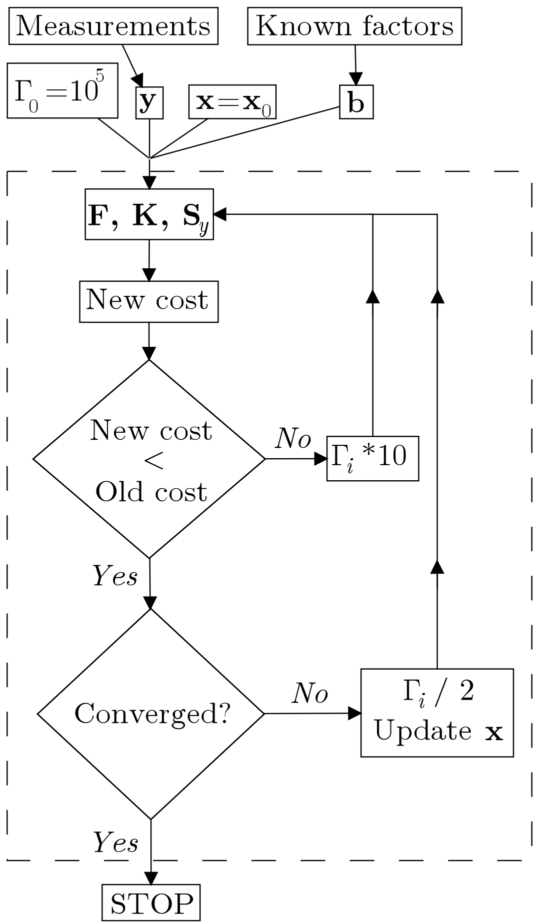

Fig. 1. Schematic of the optimal estimation retrieval algorithm.

AMTD
6, 9297–9346, 2013

Retrieval of backscatter and extinction from Raman lidar

A. C. Povey et al.

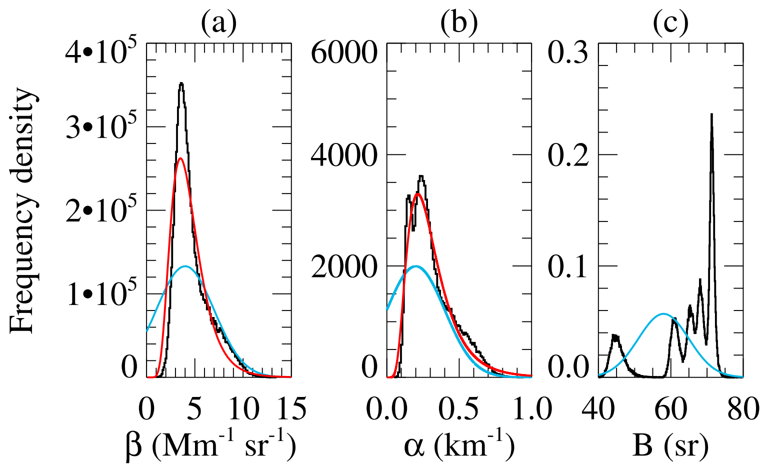

Fig. 2. A priori aerosol distributions of **(a)** backscatter, **(b)** extinction, and **(c)** lidar ratio. The blue curve represents the linear retrieval of $\boldsymbol{x}$ and the red $\ln \boldsymbol{x}$. Fit values summarised in Table 1.

AMTD
6, 9297–9346, 2013

Retrieval of backscatter and extinction from Raman lidar

A. C. Povey et al.

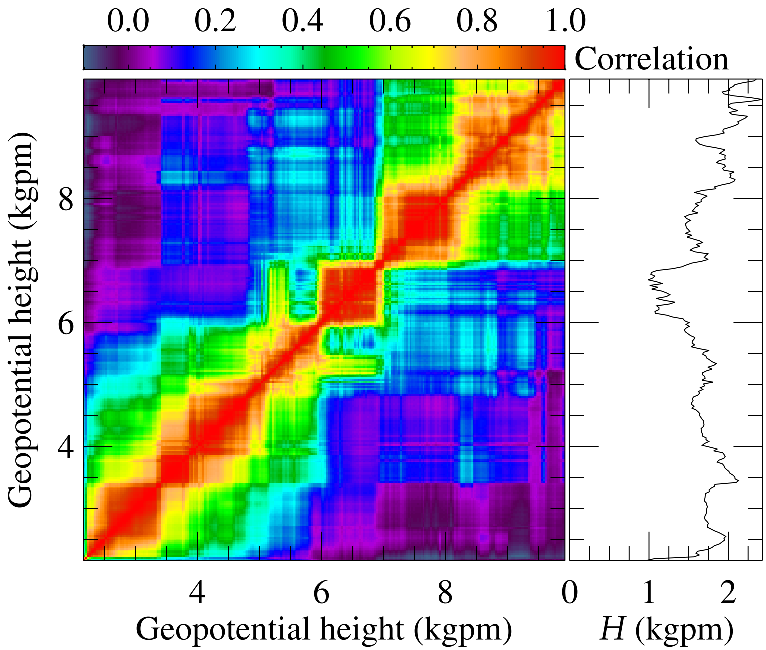

Fig. 3. The observed vertical correlation of backscatter. Left – Autocorrelation of backscatter with height, derived from 198 backscattersonde profiles collected between 1989 and 2000 at Laramie, WY, USA; Lauder, New Zealand; and Thule, Greenland. Box-like features are produced by layers of unusually large aerosol concentration during a single launch. Right – Least-squares fit of Eq. (14) to each row of that matrix for H.

Discussion Paper | Discussion Paper | Discussion Paper | Discussion Paper |

AMTD

6, 9297–9346, 2013

Retrieval of backscatter and extinction from Raman lidar

A. C. Povey et al.

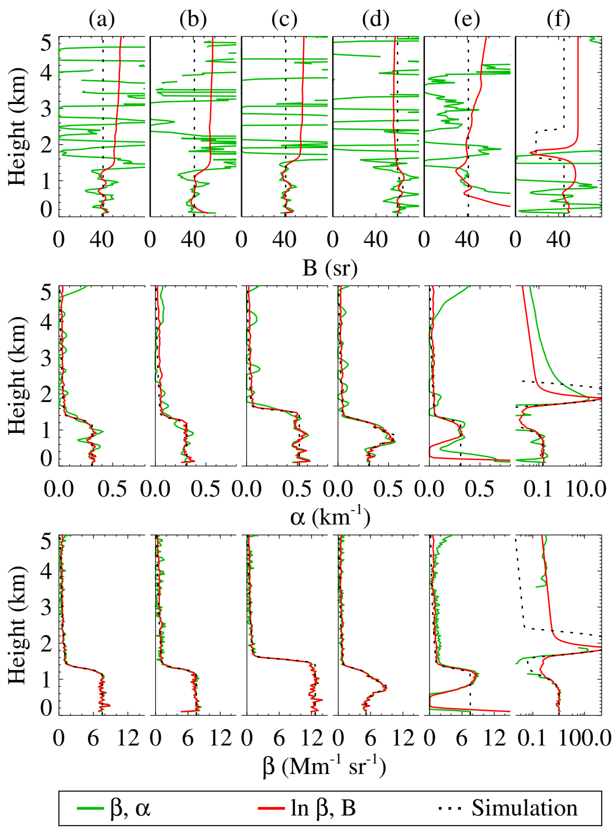

Fig. 4. Performance of the retrieval with simulated data for the linear (green) and logarithmic (red) retrieval modes. **(a)** An idealised, well-mixed PBL with $\chi = 0.50$. **(b)** As **(a)**, but observed at 20 % of the previous laser energy. **(c)** Similar to **(a)**, but with $\chi = 0.89$. **(d)** As **(a)**, but with a larger B and the addition of an aerosol layer at 800 m. **(e)** As **(a)**, but applying an incorrect nonlinear correction. **(f)** Observation of a cloud, shown on a log scale.

AMTD
6, 9297–9346, 2013

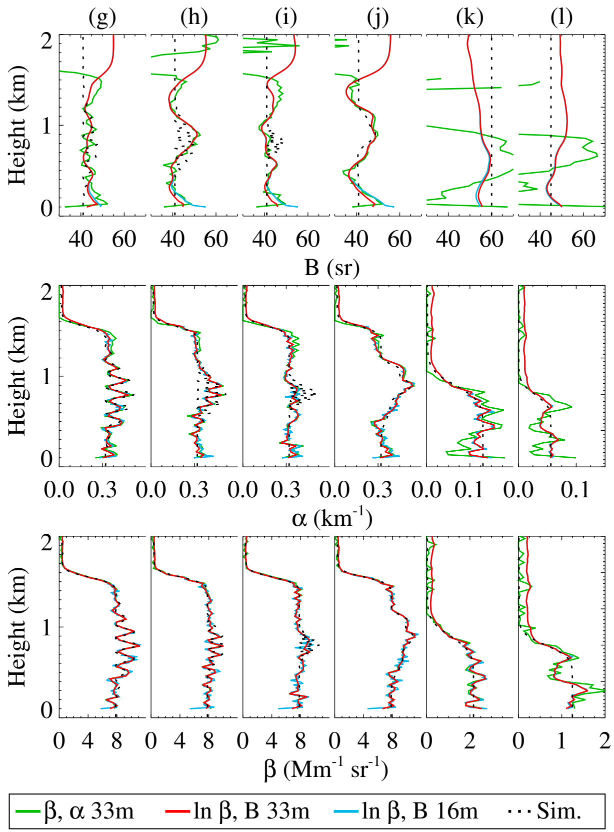

Fig. 5. As Fig. 4 but highlighting the sensitivity to fine-scale fluctuations. The blue curve shows the logarithmic retrieval at twice the previous resolution. **(g)** As **(a)**, but with the addition of sinusoidal "aerosol layers" of width 300 m. **(h)** As **(g)**, but width 200 m. **(i)** As **(g)**, but width 100 m. **(j)** As **(a)**, but including three overlapping layers. **(k)** As **(a)**, but with $\chi = 0.12$. **(l)** As **(a)**, but with $\chi = 0.04$.

AMTD
6, 9297–9346, 2013

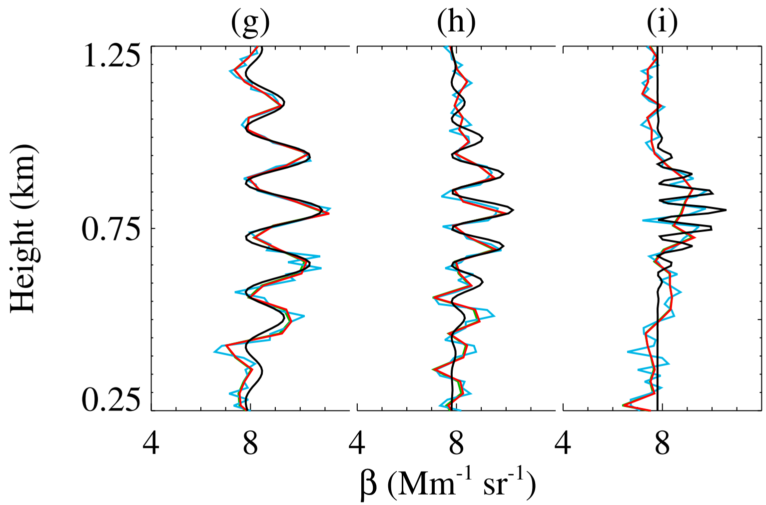

Fig. 6. A closer examination of cases (g–i) of Fig. 5, highlighting how the coarse retrievals fail to capture the smallest features and that all resolutions tend to smooth the magnitude of the peaks.

AMTD
6, 9297–9346, 2013

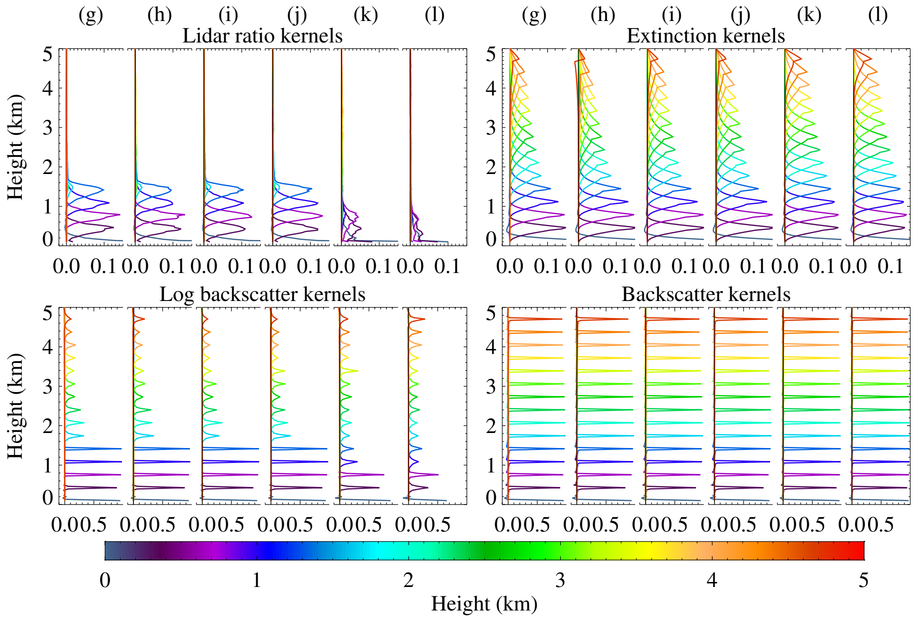

Fig. 7. Selected rows of the averaging kernels for Fig. 5, denoting the relative contribution of the true state at each height (y-axis) to the value retrieved at a height denoted by the colour. Above colour bar: Lidar ratio configuration. Below: Extinction configuration.

AMTD
6, 9297–9346, 2013

Retrieval of backscatter and extinction from Raman lidar

A. C. Povey et al.

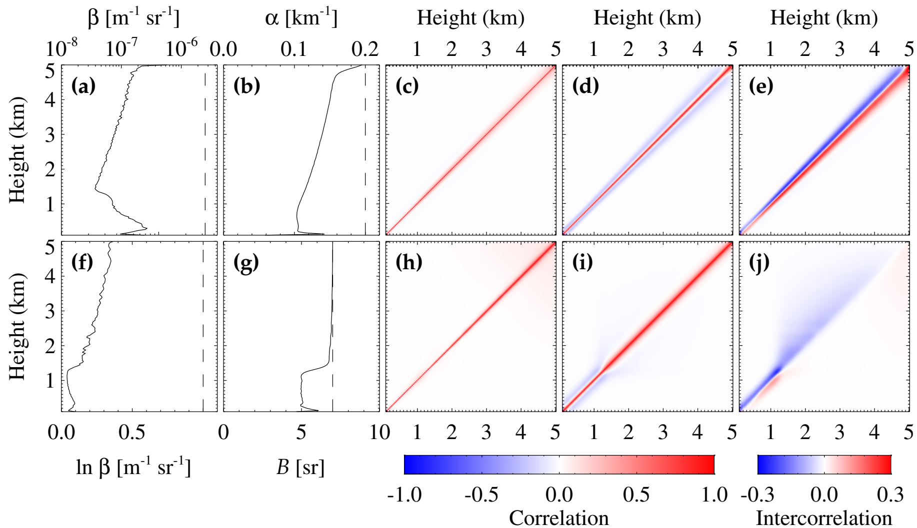

Fig. 8. Errors for the retrieval of case **(a)** by the linear and log modes (top and bottom rows, respectively). **(a)** Backscatter error. **(b)** Extinction error. **(c)** Backscatter autocorrelation. **(d)** Extinction autocorrelation. **(e)** β fvs. α intercorrelation. **(f)** Log backscatter error. **(g)** Lidar ratio error. **(h)** Log backscatter autocorrelation. **(i)** Lidar ratio autocorrelation. **(j)** ln β vs. B intercorrelation.

AMTD
6, 9297–9346, 2013

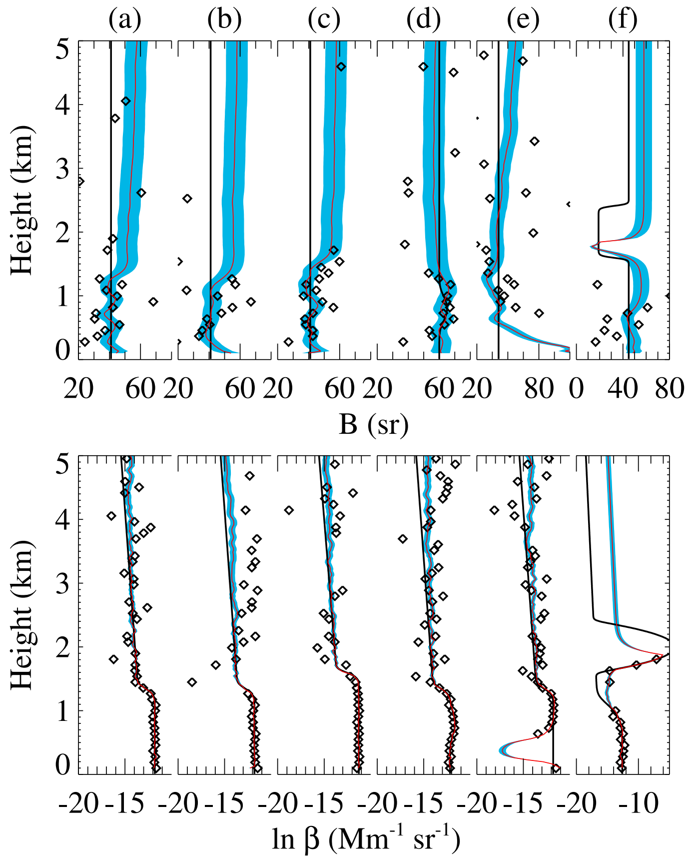

Fig. 9. Retrieval from the lidar ratio configuration (red) showing its error (blue) compared to that of the Ansmann method (diamonds) and the simulated profile (black).

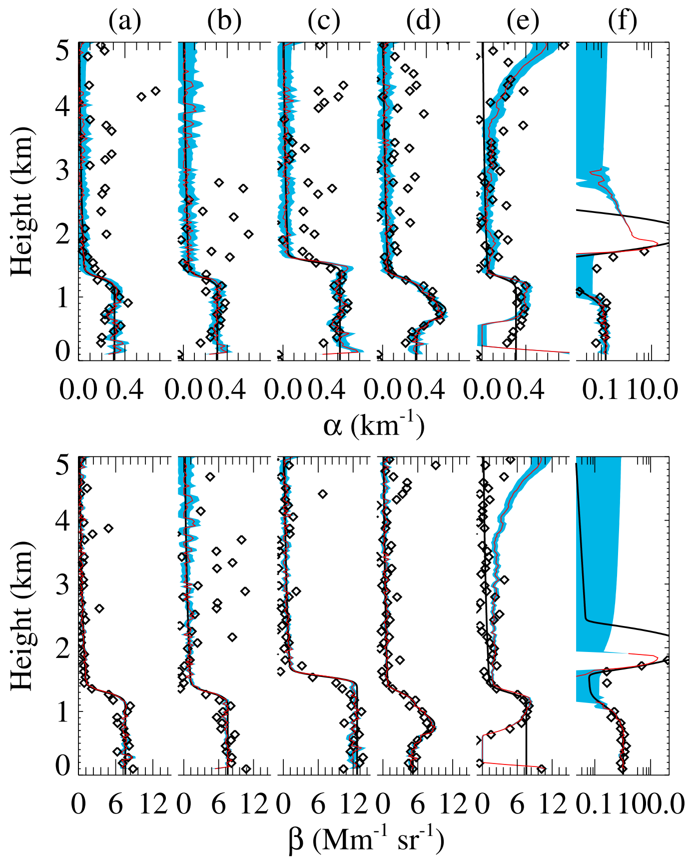

Fig. 10. As Fig. 9 but for the extinction configuration.

AMTD
6, 9297–9346, 2013

Retrieval of backscatter and extinction from Raman lidar

A. C. Povey et al.

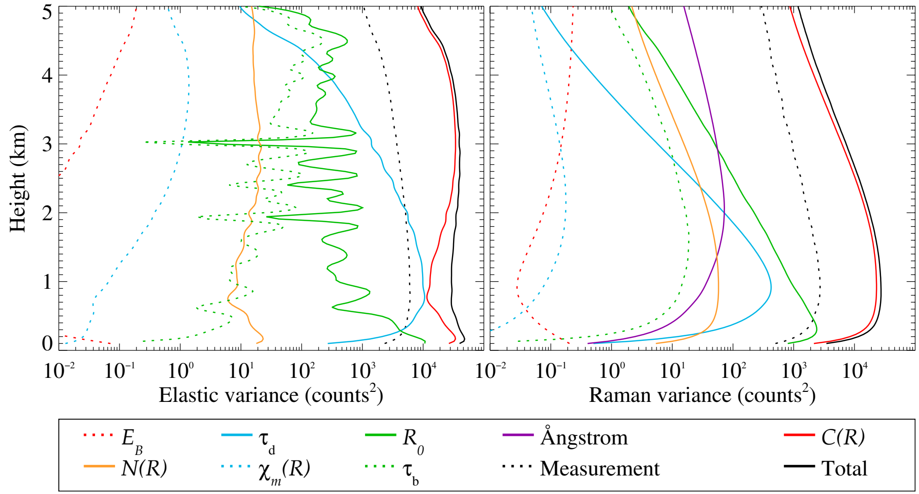

Fig. 11. The contributions of model parameters to the total retrieved variance.

AMTD
6, 9297–9346, 2013

Retrieval of backscatter and extinction from Raman lidar

A. C. Povey et al.

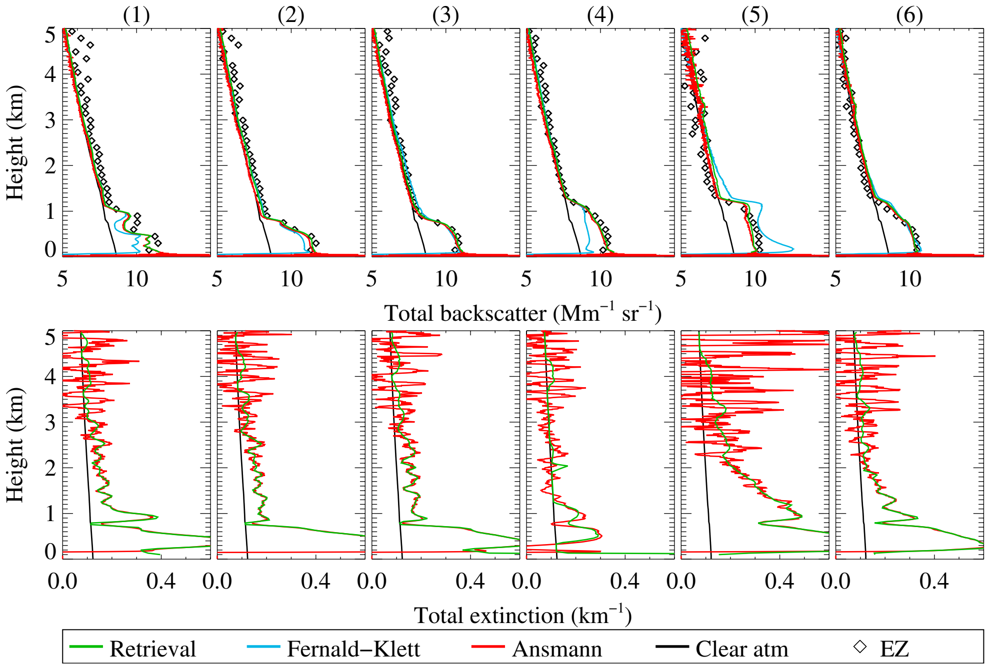

Fig. 12. Various estimates of total backscatter (top) and two-way extinction (bottom) for six analogue profiles observed by the CUV during March 2010. The attenuated backscatter coefficient $\bar{\beta}\exp[-2(\chi + \chi^{(m)})]$ reported by the EZ lidar is shown in diamonds for comparison to the total backscatter. The scattering that would be observed from a clear atmosphere is shown in black, highlighting negative α returned by the Ansmann technique.

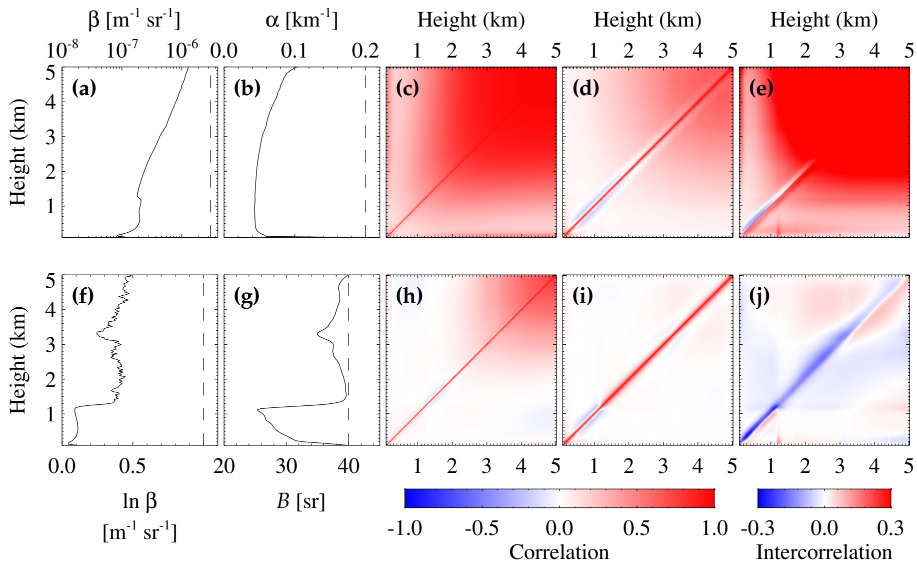

Fig. 13. As Fig. 8, but for real data from case (1) of Fig. 12. The large correlations are a function of parameter error in E_B, which affects all levels equally and becomes dominant as the SNR decreases.

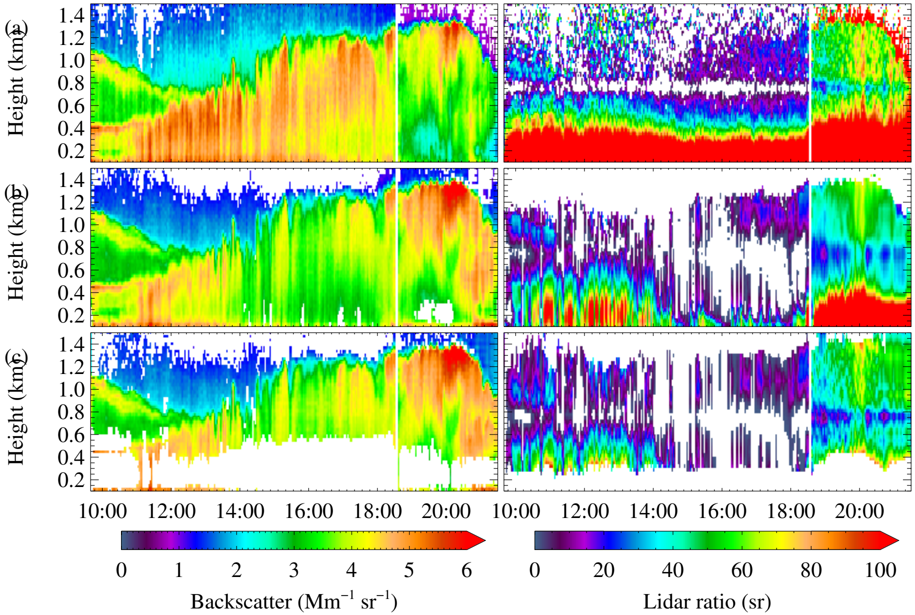

Fig. 14. The backscatter (left) and lidar ratio (right) retrieved from photon counting CUV observations on 2 March 2010. Results with an error greater than 20 % of β or 30 sr have been removed. **(a)** The Ansmann method after averaging the data over 30 m to give a similar resolution to the retrieval. **(b)** Retrieval of β and α. **(c)** Retrieval of $\ln \beta$ and B. The feature at 800 m in all lidar ratios is due to an inaccurate estimate of N.

AMTD
6, 9297–9346, 2013

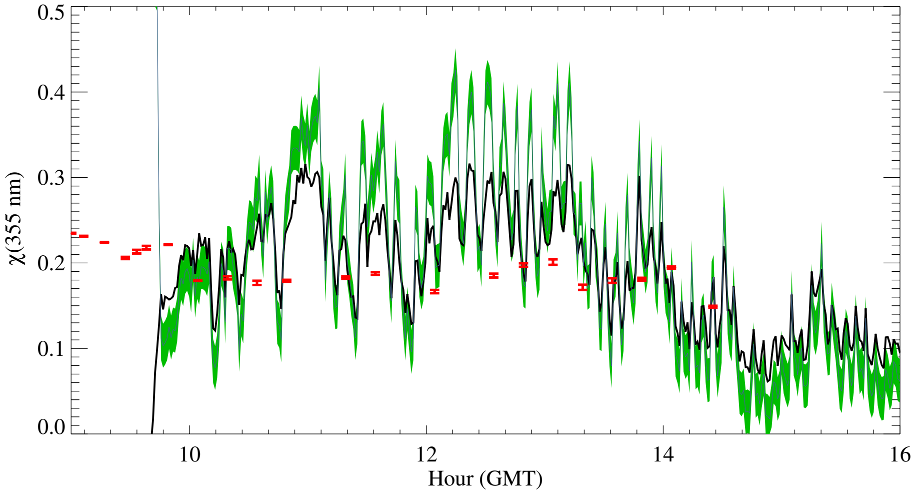

Fig. 15. Retrieved aerosol optical thickness at 355 nm (grey/green) compared to that observed by AERONET at level 2.0 (red) for 2 March 2010. The analogue Ansmann solution integrated between 0.25 and 2 km is shown in black.

AMTD
6, 9297–9346, 2013

Retrieval of backscatter and extinction from Raman lidar

A. C. Povey et al.

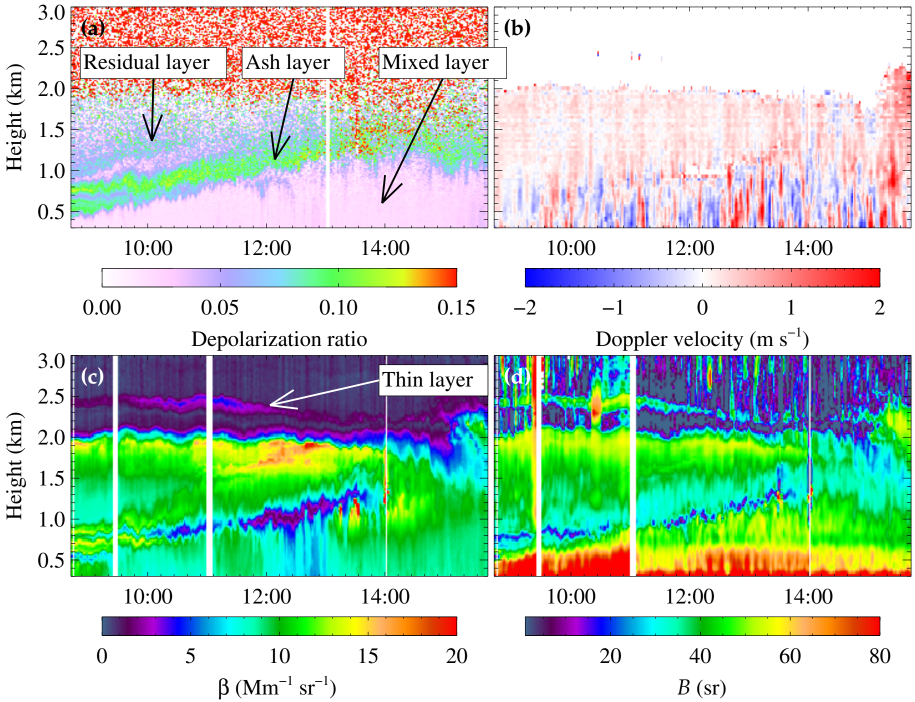

Fig. 16. Observations of the Eyjafjallajökull ash plume at CFARR on 19 April 2010. **(a)** Depolarization ratio observed by the EZ lidar. Values above 1.9 km are dominated by noise. **(b)** Vertical velocity observed by a Halo Doppler lidar. **(c)** Backscatter retrieved (in the linear mode) from CUV measurements. **(d)** Lidar ratio retrieved from same.

AMTD
6, 9297–9346, 2013

Retrieval of backscatter and extinction from Raman lidar

A. C. Povey et al.

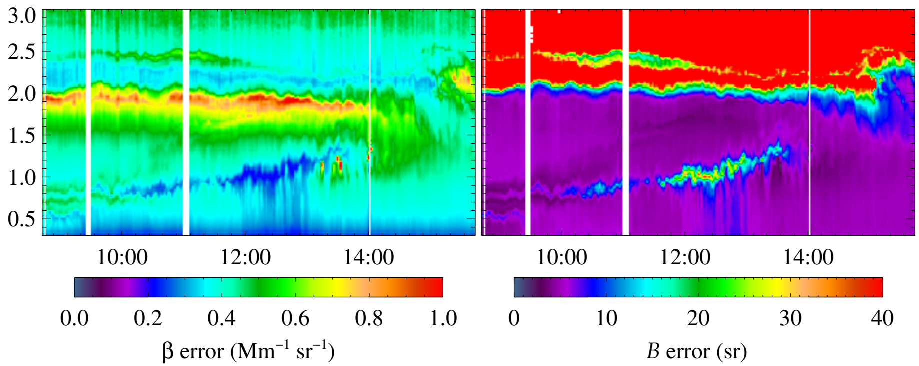

Fig. 17. Retrieved errors for plots (c–d) of Fig. 16.

AMTD
6, 9297–9346, 2013

Retrieval of backscatter and extinction from Raman lidar

A. C. Povey et al.

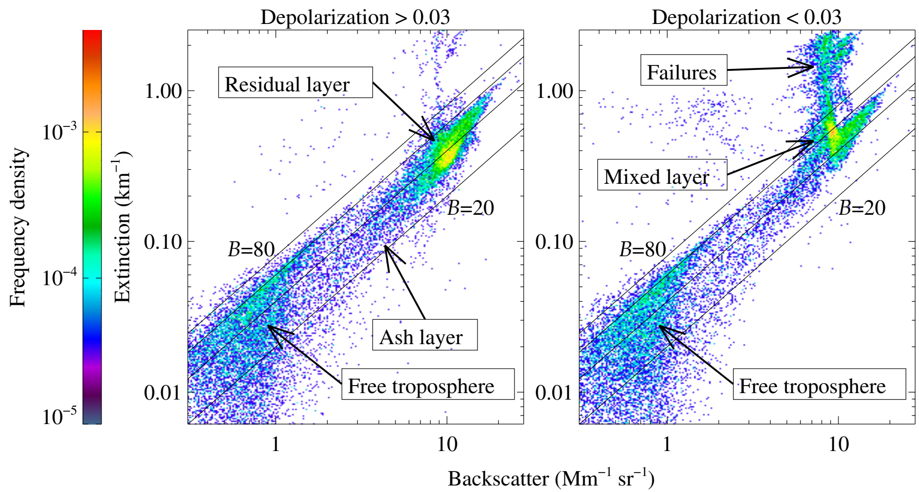

Fig. 18. Distribution of extinction and backscatter for 19 April 2010. Lines delineate lidar ratios of 20, 40, 60, and 80 sr. Left: Points observed to have a depolarization ratio > 0.03, which likely contain some quantity of ash. Right: The remaining points, corresponding to typical PBL aerosols and failed retrievals near the surface.

AMTD
6, 9297–9346, 2013

Retrieval of backscatter and extinction from Raman lidar

A. C. Povey et al.